In the format provided by the authors and unedited.

Dynamics of a massive binary at birth

Yichen Zhang[1]*, Jonathan C. Tan[2,3], Kei E. I. Tanaka [4,5], James M. De Buizer[6], Mengyao Liu[3],
Maria T. Beltrán[7], Kaitlin Kratter[8], Diego Mardones [9] and Guido Garay[9]

[1]Star and Planet Formation Laboratory, RIKEN Cluster for Pioneering Research, Wako-shi, Saitama, Japan. [2]Department of Space, Earth and Environment, Chalmers University of Technology, Gothenburg, Sweden. [3]Department of Astronomy, University of Virginia, Charlottesville, VA, USA. [4]Department of Earth and Space Science, Osaka University, Toyonaka, Osaka, Japan. [5]ALMA Project, National Astronomical Observatory of Japan, Tokyo, Japan. [6]SOFIA-USRA, NASA Ames Research Center, Moffett Field, CA, USA. [7]INAF — Osservatorio Astrofisico di Arcetri, Firenze, Italy. [8]Department of Astronomy and Steward Observatory, University of Arizona, Tucson, AZ, USA. [9]Departamento de Astronomía, Universidad de Chile, Santiago, Chile. *e-mail: yichen.zhang@riken.jp

Supplementary Information for "Dynamics of a massive binary at birth"

Supplementary Information

Binary properties if allowing for non-circular orbits. If elliptical orbits are considered, then the ranges of allowed binary orbital properties increase compared to those assuming circular orbits (Figure 3 of main paper). The minimum mass of the system for all possible elliptical orbits with an eccentricity of e is $M_{\min} = M_0/(1 + e)$, where $M_0 = 18.4 \pm 7.4\ M_\odot$ is the reference system mass assuming an edge-on circular orbit with the apparent separation of the two sources as their true separation. This provides a lower mass limit of $M_0/2 = 9.2 \pm 3.7\ M_\odot$ for the system to be bound. The total mass of the binary estimated from the free-free emissions is $22.5^{+13.5}_{-7.5}\ M_\odot$, which is consistent with this minimum mass.

Supplementary Figure 1 shows the distribution of possible binary properties in the space of total system mass and orbital period, with eccentricities $0 \leq e < 0.9$. For orbits with low eccentricities $e < 0.2$, with the estimated system mass of $22.5^{+13.5}_{-7.5}\ M_\odot$, the semi-major axis of the orbit is around 200 au, the orbital period is about $400\ \mathrm{yr} - 1000\ \mathrm{yr}$, and the inclination angle is likely to be $i > 50°$. The position angle of the orbital plane is still in a similar direction as the two sources. Some typical orbits (relative orbits of Source B with respect to Source A) with $e < 0.2$ are shown in Figure 1(c) of main paper. The constraints are weaker if the orbit has a higher eccentricity. With the estimated system mass of $22.5^{+13.5}_{-7.5}\ M_\odot$, the minimum orbital period is about 300 years with a semi-major axis of 130 au, and the maximum orbital period is about 10,000 years for $e < 0.8$ with a maximum semi-major axis of about 1,000 au.

The large-scale gas structure and possible circumbinary disk. The morphology and kinematics of the large-scale stream-like structures appear complex, as shown by the zeroth and first moment maps of CH_3OH line emission (Supplementary Figure 4a). The CH_3OH emission peak is offset from the continuum peak of the central region, extending about $0.5''$ (840 au) in the south. A velocity gradient is seen in this elongated structure with the most red-shifted velocity associated with the southern tip. In order to understand such kinematics, the position-velocity diagram is made along a cut with a position angle of $20°$, passing through the continuum peak and the elongated structure (Supplementary Figure 4b). The fact that the highest velocity and the highest velocity gradient both appear at a position $0.5''$ offset from the center can be naturally explained by infalling motion with angular momentum conserved. In such motion, the material reaches its maximum rotational velocity at the radius of centrifugal barrier where all the kinetic energy turns into rotation[1].

We construct a model to explain the kinematic features seen in Supplementary Figure 4(b). In this model, the material is infalling and rotating with angular momentum conserved. For simplicity, the motion of material is assumed to be in a plane viewed with zero inclination with the line of sight. This is supported by the fact that the large-scale structure seen in the 1.3 mm continuum and molecular line emission is missing in the mid-IR[2], indicating high extinction along this structure, which is natural for a plane of accretion that is close to edge-on. The motion can be described by

$$v_\varphi = -v_0\frac{r_0}{r},$$

(1)

$$v_r = -v_0\frac{\sqrt{r_0(r-r_0)}}{r}.$$

(2)

Such motion conserves both angular momentum and kinetic energy. Here r_0 is the innermost radius

that such infalling gas can reach with angular momentum conserved, where all the kinetic energy

turns into rotation (i.e., the centrifugal barrier), and v_0 is the rotational velocity at r_0. The shape of

the structure is assumed to follow the trajectory of such motion, which is a parabola, i.e.,

$$r = \frac{2r_0}{1 + \cos\varphi}. \tag{3}$$

Here the observer is at the direction of $\varphi = \pi/2$. The offset and line-of-sight velocity are

$$x = -r\cos\varphi, \tag{4}$$

$$V_{\text{lsr}} = V_{\text{sys}} - v_r \sin\varphi - v_\varphi \cos\varphi, \tag{5}$$

where the signs are selected to be consistent with the figure. In the model, $r_0 = 0.5''$ (840 au),

$V_{\text{sys}} = 15$ km s^{-1}, $v_0 = 7.5$ km s^{-1}. The central mass is connected to the radius and velocity of

the centrifugal barrier by

$$v_0 = \sqrt{\frac{2GM}{r_0}}, \tag{6}$$

which leads to a central mass of 27 $M_\odot$. If we use the width of the emission at $v_{\text{lsr}} = V_{\text{sys}} + v_0 = $

22.5 km s^{-1} in the PV diagram as the uncertainty of r_0 (about 20%), and assuming velocity

uncertainty of about 0.5 km s^{-1}, the uncertainty of the mass estimation is then about 24%. This

mass is close to the total mass of $22.5^{+13.5}_{-7.5}$ $M_\odot$ of the binary estimated from the free-free fluxes.

It is also consistent with the minimum mass of 18.4 ± 7.4 $M_\odot$ derived from the orbital motion for

low eccentricity orbits, and the minimum mass of 9.2 ± 3.7 $M_\odot$ for all possible bound orbits.

This example model is meant to be illustrative of the possibility that the large-scale stream is

infalling with rotation. Note, we do not try to explain all the observed structures, which is difficult

considering the clumpy distribution of the material, possible projection effects, and the filtering

of large-scale emission in our interferometric observations. Note that in the above model, the systemic velocity (the radial velocity of material at infinite distance) is 15 km s^{-1}, slightly offset from the estimates of the cloud systemic velocity ($16.5 - 18$ km s^{-1}; see Methods). Such an offset may arise if the envelope has substructures with slightly different initial velocities. The highest velocity that the infalling stream reaches is ~ 23 km s^{-1}, offset from the overall systemic velocity of $16.5 - 18$ km s^{-1} of the cloud by $5 - 6.5$ km s^{-1}. If we adopt this velocity offset for v_0, the central mass is $12 - 17$ $M_{\odot}$, which is still consistent with the minimum mass derived from the orbital motion. This mass is a lower limit if we further consider an inclination that is not fully edge-on. Besides the elongated emission peak, other more extended structures with slight velocity gradients are seen in the PV diagram, which may be part of other infalling streams with similar motions. The velocity gradients are naturally low if they are still distant from the central source.

In the model presented above, we consider that all the emission (even those toward the central sources in projection) is associated with infalling envelope structures. However, we cannot rule out the possibility that some of the emission toward the central sources in projection comes from an embedded circumbinary disk. We perform a simple estimation of the mass of any potential circumbinary material that may be present. We first convolve the high-resolution continuum emission of only the two sources with the resolution beam of the low-resolution continuum data, and then subtract the convolved map from the low-resolution continuum data. Since the continuum emission of the two sources in the high-resolution data is dominated by the free-free and dust emission in the immediate vicinities of the two sources, the residual continuum emission should only contain dust emission from surrounding materials. Within a radius of $0.5''$ (840 au) from Source

A, the total flux of the residual continuum emission is 12 mJy. Assuming a dust temperature of $50 - 500$ K (as expected from radiative transfer models of massive protostars), the continuum flux of 12 mJy corresponds to a mass of $0.26 - 0.023$ $M_\odot$. However, it is hard to confirm that this mass is indeed in a circumbinary disk. It may be belong to the parts of the infalling streams that happen to be close to the source in projection. As the position-velocity diagram shows, there is no distinct kinematic feature toward the position of the protostars to separate the circumbinary disk from the larger streams. We also note that there is no guarantee that disk fragmentation produces a substantial circumbinary ring. A substantial circumbinary disk may or may not exist after the fragmentation according to simulations[3,4].

The low-mass protostellar sources in the region. We performed a search for low-mass protostellar sources in the region using the high resolution continuum images. We identify the sources with maximum intensities $> 5\sigma$ and sizes of regions with intensities $> 4\sigma$ larger than that of 1 resolution beam. Apart from the binary, we only see three other relatively compact sources within the field of view of $< 10''$ (17,000 au) (Supplementary Figure 5). Two of these ($6''$ and $9''$ away from the binary) may be protostars (panels b and c). One other ($9''$ away from the binary) does not have a point-like core, so we do not expect it to be a protostellar source (panel d). The masses of these condensations are 0.022, 0.014, and 0.25 $M_\odot$, respectively, assuming 30 K dust temperature. In addition to these three sources, there is also some emission to the south of the binary (panel e). However, it appears to be extended and is part of the elongated structure reaching to about $0.5''$ south of the binary seen in the low-resolution data. Therefore we also do not expect it to be a protostar. Thus our observations are sensitive to the presence of low-mass protostellar sources,

but we only see very limited number of such sources in the region around the binary. We consider that the lack of other protostellar sources in the immediate environment of the binary (i.e., the next closest source in projection is many (~ 50) binary orbital separations away), is evidence against a turbulent fragmentation scenario for formation of the binary.

1. Sakai, N. et al. Change in the chemical composition of infalling gas forming a disk around a protostar. *Nature* **507**, 78-80 (2014).

2. De Buizer, J. M. et al. The SOFIA massive (SOMA) star formation survey. i. overview and first results. *Astrophys. J.* **843**, 33 (2017).

3. Krumholz, M. R., Klein, R. I. & McKee, C. F. Radiation-hydrodynamic simulations of collapse and fragmentation in massive protostellar cores. *Astrophys. J.* **656**, 959-979 (2007)

4. Kratter, K. M., Matzner, C. D., Krumholz, M. R. & Klein, R. I. On the role of disks in the formation of stellar systems: a numerical parameter study of rapid accretion. *Astrophys. J.* **708**, 1585-1597 (2010).
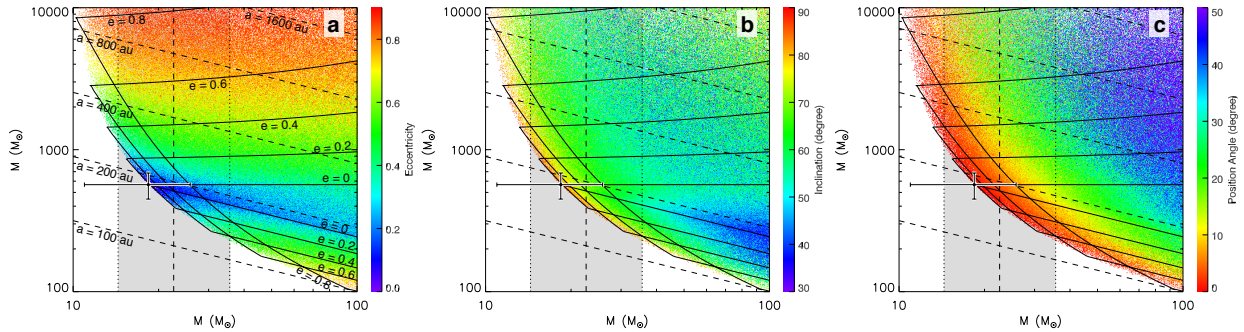
Supplementary Figure 1: **The distribution of the possible binary properties in the space of system mass and orbital period. a:** The color shows the eccentricity of the orbits. **b:** The color shows the inclination of the orbital plane relative to the plane of sky. **c:** The color shows the position angle of the intersection line between the orbital plane and the sky plane, with respect to the position angle of the line connecting Sources A and B. All possible elliptical orbits with eccentricities from 0 to 0.9 are considered. The data point and error bars correspond to the system mass, orbital period, and their 1σ uncertainties, assuming an edge-on circular orbit with the apparent separation of the two sources as their true separation. The dashed vertical line and the shaded regions indicate the system mass and its uncertainties derived from the free-free emissions. The dashed diagonal lines show the locations of orbits with different semi-major axes, as labelled in panel a. The solid lines encircle the regions for eccentricities of $e = 0$, 0.2, 0.4, 0.6, and 0.8 (labelled in panel a).
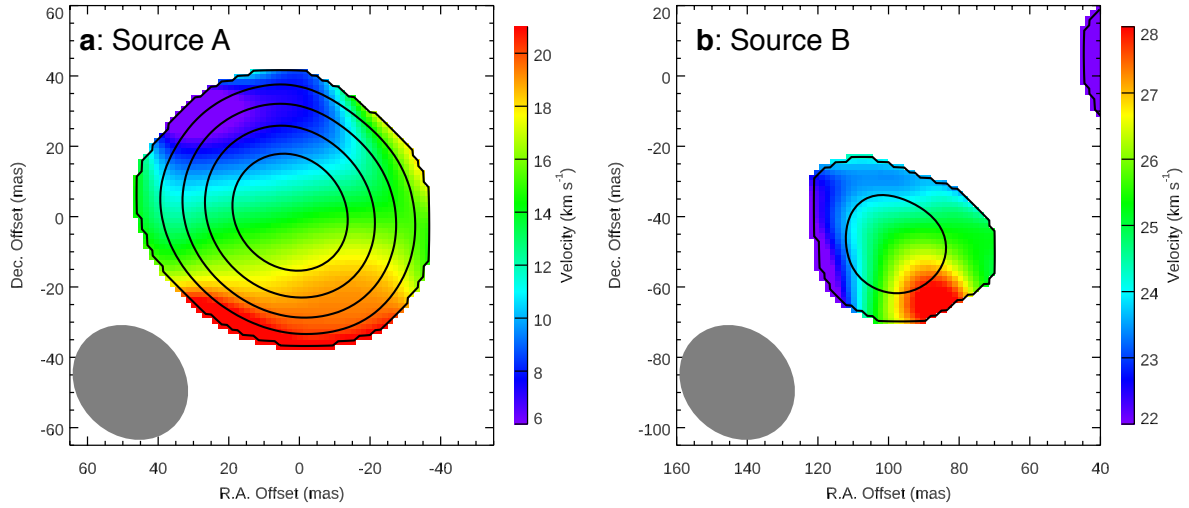
Supplementary Figure 2: **The moment maps of the H30α emission in Source A (panel a) and B (panel b).** The moment 0 maps (integrated emission) are shown in the black contours and the moment 1 maps (intensity-weighted mean velocities) are shown in the color scale. The moment 0 map in panel a is integrated in the velocity range of -30 km s^{-1} $< V_{\rm lsr} < 55$ km s^{-1}, and the contour levels are $5\sigma \times 2^n$ ($n = 1, 2, 3, ...$) with $1\sigma = 13$ mJy beam^{-1} km s^{-1}. The moment 0 map in panel b is integrated in the velocity range of -10 km s^{-1} $< V_{\rm lsr} < 60$ km s^{-1}, and the contour levels are $5\sigma \times 2^n$ ($n = 1, 2, 3, ...$) with $1\sigma = 14$ mJy beam^{-1} km s^{-1}. The synthesized beam is shown in the bottom-left corner.
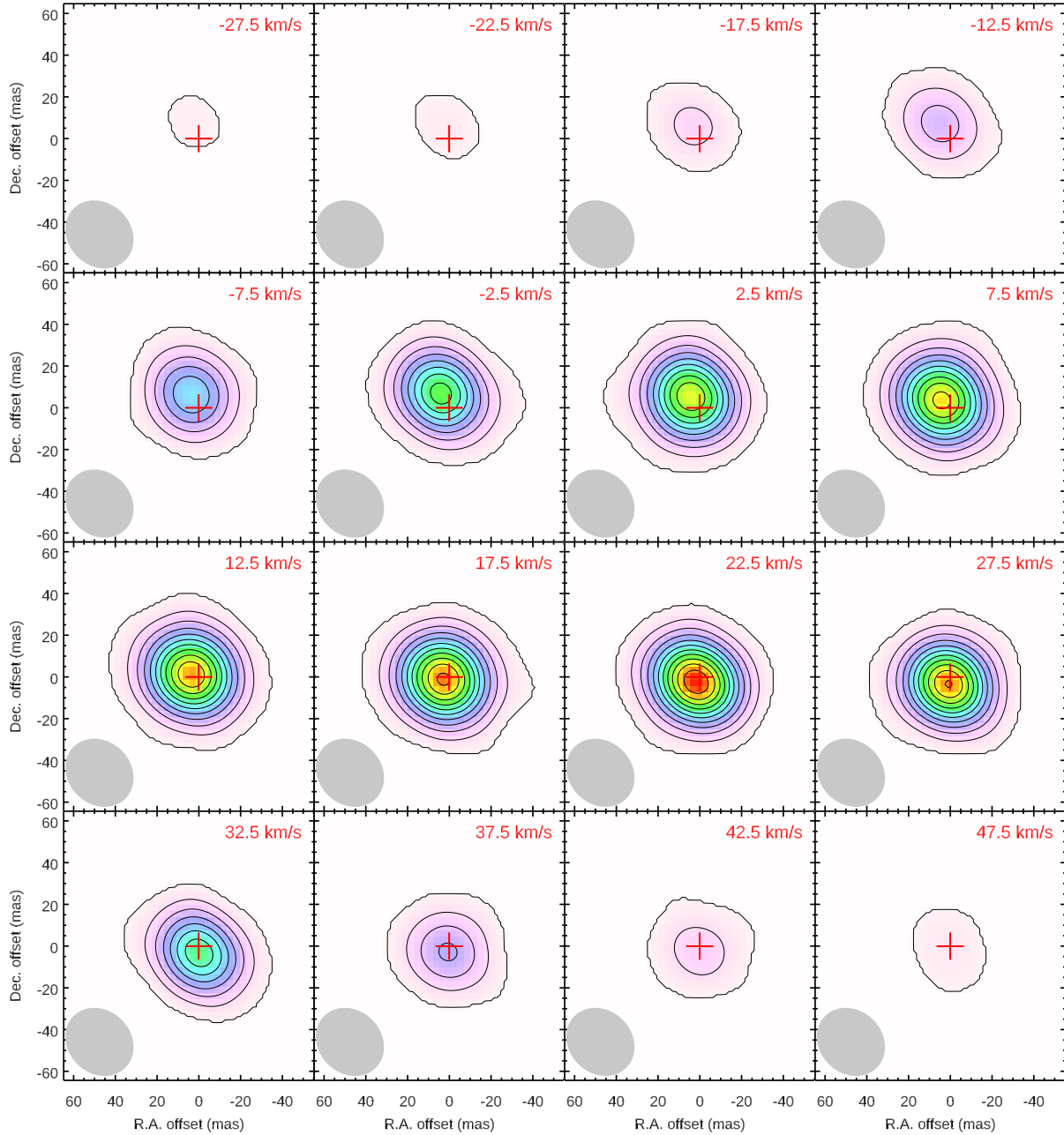
Supplementary Figure 3: **The channel maps of the H30α emission in Source A.** The channel width is 5 km s^{-1} and the central velocities of the channels are labeled in the upper-right corners of the panels. The contours start at 5σ and have an interval of 10σ with $1\sigma = 17$ K (0.8 mJy beam^{-1}). The synthesized beam is shown in the bottom-left corner of each panel. The red cross marks the position of the continuum peak.
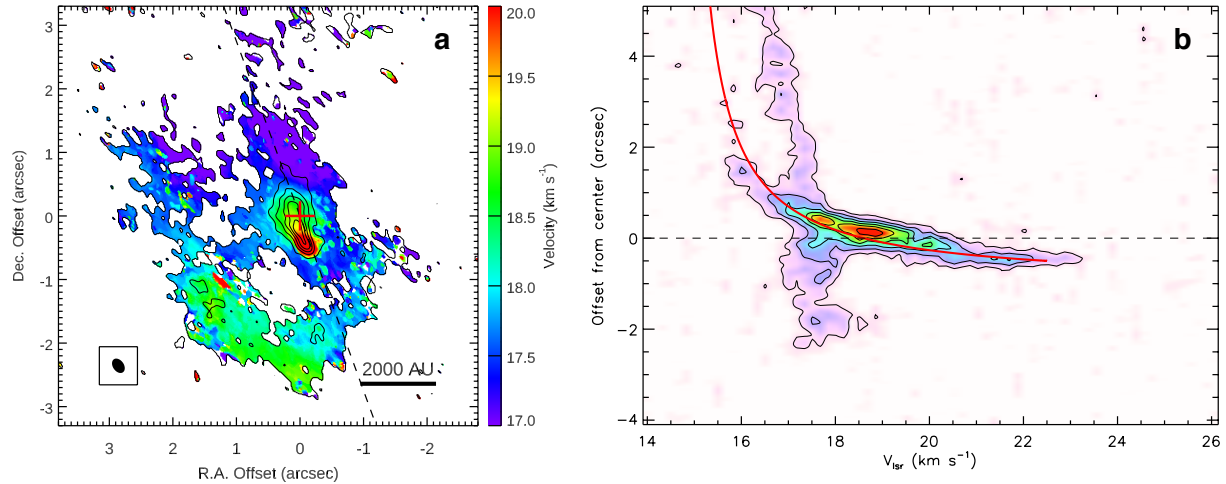
Supplementary Figure 4: **The kinematics of the large scale CH₃OH emission. a:** The moment maps of the large scale CH$_3$OH $4(2,2)-3(1,2)$ emission. The moment 0 map (emission integrated from $V_{\rm lsr} = 15$ to 23 km s^{-1}) is shown in the black contours and the moment 1 map (intensity-weighted mean velocities) is shown in the color scale. The contour levels start at 3σ and have intervals of 6σ ($1\sigma = 7$ mJy beam^{-1} km s^{-1}). The synthesized beam, shown inside the bottom-left square, is $0.25'' \times 0.17''$. The red cross marks the position of the continuum peak. The dashed line indicates the cut for the position-velocity diagram shown in panel b. **b:** The position-velocity diagram of the CH$_3$OH emission along the cut shown in panel a. The cut width is $0.5''$. The contour levels start at 3σ and have intervals of 3σ ($1\sigma = 4$ mJy beam^{-1}). The red curve is a model for explaining the kinematics (see Supplementary Discussion).
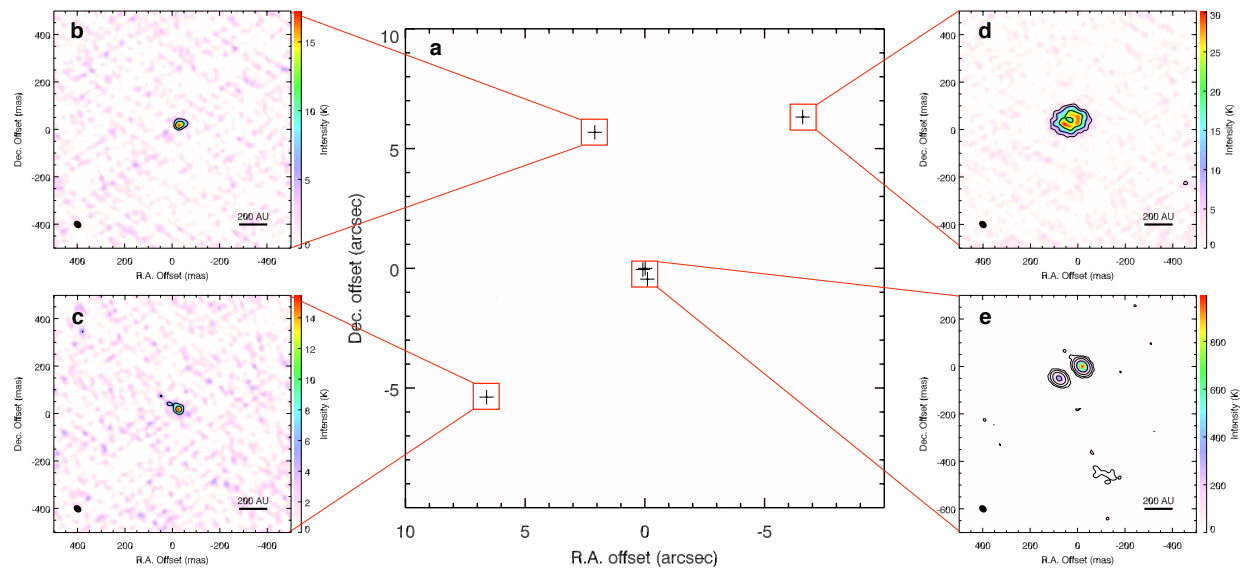
Supplementary Figure 5: **Compact continuum sources identified in the high-resolution data.**
a: continuum map of the region $< 10''$ from the central sources, with the crosses marking the
identified continuum sources. **b**−**e:** Zoom-in views of the identified continuum sources.
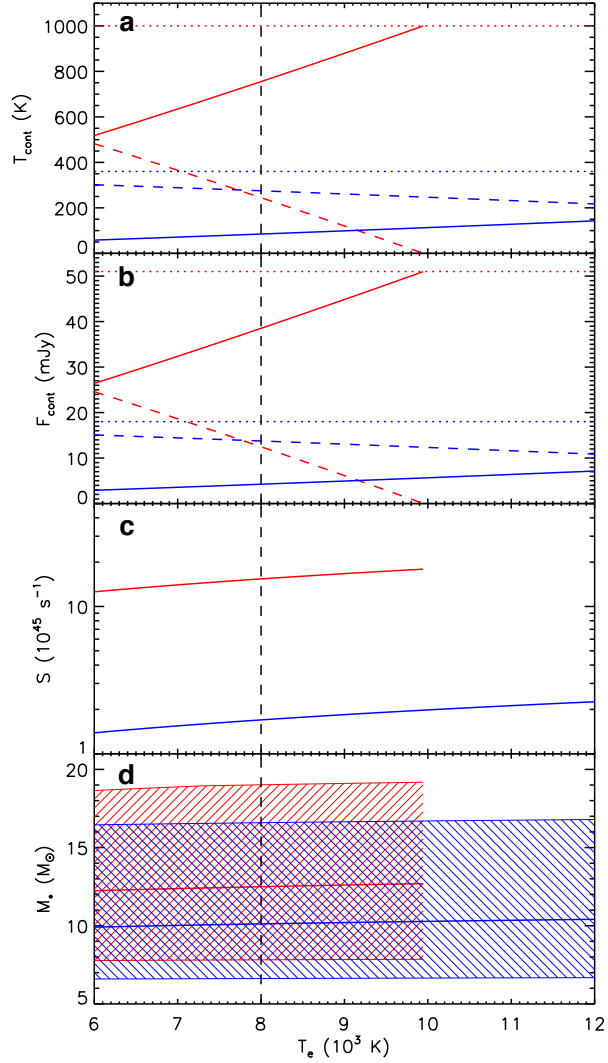
Supplementary Figure 6: **Dependence of the estimated free-free peak intensities (panel a), fluxes (panel b), ionizing photon rates (panel c), and protostellar masses (panel d) of the two sources on the assumed ionized gas temperature.** The red and blue colors are for Source A and B, respectively. The solid, dashed, and dotted lines in panels a and b are for the free-free, dust continuum, and total continuum emissions. The solid lines in panel d are estimated ZAMS stellar masses, and the shaded regions indicate the ranges of protostellar masses calculated from different accretion histories. The vertical line indicates the temperature of 8000 K of ionized gas, which is used as the fiducial case in the main text.